Asian Journal of Chemistry; Vol. 37, No. 3 (2025), 641-652

ASIAN JOURNAL OF CHEMISTRY

https://doi.org/10.14233/ajchem.2025.33082

# Enhancing the Photocatalytic Activity of Co-precipitation Synthesized $Fe_3O_4$/ZnO Nanocomposites for Rhodamine B Degradation

N.S.M. KUBHEKA[1], E.N. NXUMALO[1], M. MANAGA[1] and M.J. MOLOTO[1,2,*]

[1]Institute for Nanotechnology and Water Sustainability, College of Science, Engineering and Technology, University of South Africa, Roodepoort 1709, South Africa
[2]Department of Chemistry, Faculty of Applied Sciences, Durban University of Technology, Steve Biko road, Musgrave, Durban, South Africa

*Corresponding author: Tel: +27 (0)636934514; E-mail: Makwena.moloto@outlook.com

*Received*: 26 November 2024; *Accepted*: 6 February 2025; *Published online*: 28 February 2025; AJC-21921

Severe global issues with a great deal of water scarcity and contamination by organic materials such as dyes dominate the challenges of the 21st century in environmental-related areas. Recently, there has been a plethora of opportunities for nanotechnology to produce multifunctional nanocomposites with high surface-to-volume ratios and distinctive surface functions to address these contaminants. This study report on the synthesis of $Fe_3O_4$/ZnO nanocomposite through co-precipitation method and investigate of degradation of rhodamine B (RhB) dye under visible irradiation. The prepared different ratios (1:1, 1:2 and 2:1) of $Fe_3O_4$/ZnO nanocomposites were characterized using various microscopic and spectroscopic techniques. The SEM images illustrated that the nanomaterials had an irregular flake-like shape and TEM images depicted well defined core-shell $Fe_3O_4$/ZnO nanocomposite structures. The FTIR and Raman spectroscopic results confirmed the functional groups and the different vibrational modes of the composite nanoparticles. The UV-Vis, PL spectra and Tauc plot revealed that the molar ratio had band gap energies below 3.0 eV. The 1:1 ratio was highly mesoporous (94.36 $m^2/g$) with distinct vibrational mode features of core-shell structures and a band gap energy of 2.85 eV, making it a suitable photocatalyst. A comparison of the photodegradation of the 1:1 $Fe_3O_4$/ZnO nanocomposite ratio using visible and solar irradiation light revealed that RhB exhibited a high degradation efficiency of 83.81% under visible light.

**Keywords: Nanocomposites, Multifunctional, Contaminants, Adsorption, Photocatalyst.**

## INTRODUCTION

The deterioration of water quality and contamination remains a prominent issue up to date. Preservation of environmental remediation is still an on-going topic amongst researchers. Several industries such as textile, cosmetic, pharmaceutical and paper manufacturing make use of azo dyes that are dsicharged into the environmental water sources [1]. The presence of the dyes in water poses a risk to the ecosystem because these dyes are resistant to biodegradation due to the complexity of their structures interlinking azo bonds [N=N] and their photostability. The presence of organic dyes such as rhodamine B (RhB) in wastewater also poses a risk to human health that can be mutagenic, carcinogenic and neurogenic. Therefore, the removal of this dye is vital for environmental remediation and sustainability [2]. Rhodamine B dye is a cationic azo dye that degrades less effectively under both acidic and basic conditions and highly effective under neutral conditions [3]. Many other traditional methods have been used (*i.e.* adsorption, membrane separation techniques, chemical precipitation, ion exchange, electrodialysis) for the removal of colourants present in water but, photocatalytic degradation is considered the most effective method for eliminating RhB dye present in wastewater [4]. It is cost-effective, ecofriendly and capable of complete mineralization of contaminants into non-toxic species.

The utilization of enhanced heterojunction semiconductors is a feasible approach for the efficient degradation of dyes [5,6]. The bench marking of semiconductors such as zinc oxide which are widely used by scientists due to its high surface-to-volume ratio, photosensitivity, quantum efficiency, chemical stability and non-toxic properties [7]. Magnetite has a high saturation magnetization for complete recovery process and good stimulation for photodegradation of persistent organic pollutants [7,8]. Tailoring of metal oxides such as magnetite ($Fe_3O_4$) and zinc oxide (ZnO) to produce nanocomposites is a feasible approach for enhancing the photocatalytic activity of heterojunctions.

The synergistic effects from the combination of $Fe_3O_4$ and ZnO can result in high adsorption efficiencies for organic pollutants and enhanced electron-hole pair separation during photodegradation under visible light [8-10]. Other factors such as choice of synthesis approach, chemical stability, structural architecture, pH of the semiconductors attributing to particle aggregation under basic conditions and band positions should all be considered when producing an effective nanocomposite photocatalyst.

The degradation of cationic dyes under visible light using $Fe_3O_4$/ZnO nanocomposites has been studied by several researchers [11-14]. Although there are limited studies focusing on the degradation of RhB through co-precipitated $Fe_3O_4$/ZnO nanocomposites under visible light irradiation. Studies conducted previously illustrate that $Fe_3O_4$/ZnO nanocomposites have good properties of adsorption and photodegradation of various contaminants for environmental remediation, respectively [15]. The photocatalytic activity of RhB was studied under visible light using various nanocomposites. $Fe_3O_4$/ $TiO_2$ prepared *via* the hydrothermal method showed enhanced degradation efficiency of 91 % for RhB within 120 min under visible light, attributed to increased light absorption and improved electron-hole pair [10]. The prepared ferromagnetic multifunctional $Fe_3O_4$ core-shell nanostructures with ZnO prepared through co-precipitation formed hetero-epitaxially on top of the $Fe_3O_4$ nanoparticle core. The $Fe_3O_4$ showed superparamagnetic activity in an applied magnetic field at room temperature. It was further reported that the synthesized $Fe_3O_4$/ZnO remained magnetic and from the photoluminescence results it showed a strong photoresponse, indicating its potential use for photocatalytic application [16]. The synthesis of monodispersed microrods of $Fe_3O_4$/ZnO nanoparticles for water treatment applications using the one-step synthesis method reported that $Fe_3O_4$/ZnO heterostructures demonstrate the highest removal efficiency and photocatalytic activity, degrading RhB to 100% after 40 min in the presence of an oxidant compared to pure ZnO and $Fe_3O_4$ structures [7].

The simple surfactant-free fabrication technique utilized to synthesize ZnO/$Fe_3O_4$ composites compared ZnO and ZnO/ $Fe_3O_4$. It was confirmed that the ZnO/$Fe_3O_4$ composites demonstrated improved photocatalytic performance for the degradation of phenol and the activation of *E. coli* under visible light irradiation [17]. The hydrothermally prepared core-shell $Fe_3O_4$@ ZnO@ZIF-8 nanocomposites efficiently degraded 98% of RhB within 100 min with a reaction rate of 0.0292 $min^{-1}$ [9]. The magnetically separable $Fe_3O_4$@ZnO nanocomposites reported that the performance of the prepared catalyst performed better under UV light irradiation (37 % of RhB, 240 $min^{-1}$) compared to visible light irradiation [12]. All the above findings illustrate the different methods of synthesis approach that produced the desired nanocomposites for the efficient degradation of efficient RhB degradation under visible irradiation. Minimal research studies report on the synthesis of $Fe_3O_4$/ZnO nanocomposites synthesized *via* the co-precipitation method for the efficient degradation of RhB dye contaminants under visible irradiation. Thus, the co-precipitation method is considered a simple approach for synthesizing nanocomposites since it allows control over particle size, morphology and composition, which directly influence the properties of the nanocomposites and its intended application. Therefore, this study focused on tuning the structural properties, functional groups, band gap energies, separation properties and electron charge carriers of the encapsulated core-shell $Fe_3O_4$/ZnO nanocomposite prepared *via* co-precipitation method for the efficient degradation of the rhodamine B dye.

## EXPERIMENTAL

Ferric(III) chloride (≥ 97%), ferrous salts (≥ 99%), glycine, diethylene glycol, zinc acetate dihydrate (≥ 98%), ammonium hydroxide (25%), ethanol, sodium hydroxide, hydrochloric acid (ACS reagent 37%), polyvinylidene fluoride (PVDF, m.w. = 534000), ferrocyanide ($K_4Fe(CN)_6{\cdot}10H_2O$, 98%), ferricyanide ($K_3Fe(CN)_6$, 99%), potassium chloride (KCl, 99%) and rhodamine B dye were purchased from Merck.

**Experimental procedure:** Different ratios (1:1; 1:2 and 2:1) of the magnetite/zinc oxide nanocomposites were prepared by the co-precipitation method under pH basic conditions. The molar ratio (1:2) of $FeCl_2{\cdot}4H_2O$ and $FeCl_3{\cdot}6H_2O$ was agitated at 80 ºC in an aqueous medium under $N_2$ gas atmosphere for 30 min. Ammonium hydroxide (25%) was added after the formation of black magnetite nanoparticle precipitates. The $Fe_3O_4$ solution was refluxed at 100 ºC for 1 h. Then, $Zn(CH_3CO_2)_2{\cdot}2H_2O$ was deposited into the mixed solution then 20 mL of diethylene glycol was added. The composite solution was agitated slowly and heated to reflux. The $Fe_3O_4$/ZnO nanocomposite formed precipitates once maximum reflux temperature was reached, the reaction mixture solution was agitated for another 0.5 h under reflux temperature. The pH of the solution was adjusted using 0.1 M of NaOH and HCl. The attained samples were washed with ethanol several times and deionized water. Then, dried at room temperature for 24 h and placed in an oven at 70 ºC. Thereafter, samples were calcined at 400 ºC for 2 h. Magnetite (ferric salts; 1:2 molar ratio) and ZnO (0. 1 M) nanoparticles were synthesized separately using the same method.

**Photocatalytic experiments:** The photocatalyst (20 mg) was added into 80 mL of RhB (10 ppm) aqueous solution under continuous stirring. This study was conducted under visible light source utilizing a 4D model photoreactor (250 W HPMVL, Thane, India) at ambient temperature condition (25 ºC). Before the commencement of the degradation experiments. The mixture was stirred for 0.5 h in dark to achieve equilibrium between adsorption-desorption between the dye and the photocatalyst ($Fe_3O_4$/ZnO). After equilibrium is reached, the degradation process is monitored by measuring the absorbance of RhB dye using the UV-vis spectrometer. The same method as above was used to prepare the photocatalyst for solar irradiation studies. A 300 W xenon lamp solar simulator (HAL-350) was used to determine the irradiation process. A microfilter of 0.45 μm was used to collect 3 mL aliquots at different time intervals.

**Electrochemical measurements:** The electrochemical measurement was conducted by drop casting 2 mg PVDF, 10 mg sample in 3 mL ethanol on the working electrode and placing the working electrode in 50 mL of 5 mM ferro/ferricyanide as electrolyte.

**Characterization:** The morphological characteristics of the bulk modified nanoparticles was observed using scanning electron microscopy (FESEM, JEOL JSM-IT300) equipped with Oxford Instruments EDX system. Transmission electron microscope (JEOL JEM-2100) operating at 200 kV was used to observe the different ratios of the modified $Fe_3O_4$/ZnO nanoparticles. Malvern Instruments Inc. Zeta Sizer, model Nano-ZS, was used to measure the dispersion properties of nanoparticles. The Perkin-Elmer Frontier FT-IR spectrometer (spectrum 100 spectrometer) was utilized to confirm the functional groups of the nanoparticles using KBr method. Raman spectroscopy (WITec alpha300 confocal Raman microscope) was used to measure the vibrational modes of the sample. The Spectrophotometer Lamda 6505 was used to obtain the UV-vis diffuse reflectance spectra of the nanoparticles and nanocomposites. Photoluminescence analysis were conducted using a Kimon-1 K (Japan) to obtain the emission peaks of the nanoparticles. X-ray photoelectron spectroscopy (Thermo ESCAlab 250Xi spectrometer) was utilized for XPS analysis and possesses Al *K*α (1486.7 eV) monochromatic irradiation source. XPS study was used to determine the interaction between the bulk nanoparticles and the composite nanoparticle ratios. BET (HORIBA SA-9600 instrument) was used to evaluate the surface areas of the modified $Fe_3O_4$/ZnO nanoparticles by nitrogen adsorption–desorption isotherms on Tristar II3020 nitrogen adsorption apparatus (Micromeritics Instruments, USA). The electrochemical properties were measured using the Metrohm AUTOLAB-302N Potentiostat/Galvanostat coupled with a counter electrode (Pt wire), reference electrode (Ag/AgCl in 3 M KCl) and the working electrode.

## RESULTS AND DISCUSSION

**Morphological and structural properties of $Fe_3O_4$/ZnO nanoparticles:** Fig. 1 shows the SEM and TEM inset images of the separately prepared (a) $Fe_3O_4$ and (b) ZnO nanoparticles. TEM results showed that the calcined $Fe_3O_4$ nanoparticles were not definite cubic shaped with approximately particle size of 10 nm and ZnO nanoparticles had a spherical morphology with particle size of 0.2 µm. Both SEM and TEM (inset) images of the separately prepared bulk nanoparticles showed that the $Fe_3O_4$ nanoparticles were agglomerated and ZnO nanoparticles were aggregated. According to the pourbaix diagram of ZnO and $Fe_3O_4$ nanoparticles, these bulk nanoparticles are produced between pH 8-12 and between pH 2-9, although it is generally known that magnetite and hematite phases of iron oxide phases are superimposed between those pH ranges [18,19]. Therefore, the high calcination temperature attributes to the formation of stable cubic $Fe_3O_4$ and spherical ZnO nanoparticles. TEM images of Fig. 1c,e,g shows that the different molar ratios of modified $Fe_3O_4$/ZnO nanocomposites are aggregated and agglomerated with cubic and spherical-like shapes, predominantly the 1:1 and 2:1 ratio. It is observed that the combination of the bulk nanoparticles results in the formation of core-shell nanocomposite structures with the darker core as $Fe_3O_4$ and the lighter shell as ZnO. The addition of capping agents such as glycine and diethylene glycol influenced the aggregation of the nanoparticles and accelerated the nucleation of ZnO metal clusters. The produced core-shell nanocomposites structure is produced through the coalescence of the small ZnO nanoparticles that converged into larger particles entrapping $Fe_3O_4$ nanoparticles. The observed aggregation of the ZnO nanoparticles is also due to the increment of glycine- $Fe_3O_4$ composition correlated with literature [20]. Therefore, this suggests that the different $Fe_3O_4$/ZnO nanocomposites molar ratios enhanced the encapsulation of interfacial chemical interaction and morphological architecture of the nanocomposites therefore enhancing the mass transport of photogenerated electrons for efficient degradation of RhB dye molecules. The basic pH condition and calcination temperature of 400 ºC attributed to the distinct formulated core-shell structures of $Fe_3O_4$/ZnO nanocomposites. The average particle diameter size of the different ratios (1:1, 1:2 and 2:1) was determined using the imageJ software and found to be 23.23, 34.14 and 53.03 nm. The observed increase in particle size suggests that the core-shell morphology of the 1:2 and 2:1 ratio's is less crystalline than the 1:1 ratio of $Fe_3O_4$/ZnO nanocomposites. The chemical composition of the modified $Fe_3O_4$/ZnO nanoparticles was determined using EDX analysis (Fig. 1d,e,h), which confirmed the presence of Fe, Zn and O peaks. The carbon (C) peaks are attributed by the carbon coating during sample preparation and the chlorine (Cl) is attributed to the smaller quantities of unreacted ferric chloride salt and HCl used to stabilize the pH of the nanoparticle solution. The EDX analysis confirmed the elemental composition peaks of the nanocomposites and it was observed that the samples had some impurities.

Generally, the higher the Z-average value indicate higher degree of agglomeration for smaller particles into bigger particles [19]. The average Z value of the nanocomposites, 1:1, 1:2 and 2:1 molar ratios was found to be 961.7, 1184 and 304.5 nm, respectively (Fig. 2). The lowest average Z value for the 2:1 observation correlates with the agglomerated morphology of the nanocomposites as observed from the TEM analysis (Fig. 1).

**FTIR and Raman spectral studies:** The FTIR spectrum (Fig. 3a) confirmed the presence of characteristic stretching vibration peaks of M-O bonds typically observed in the region less than the 1000 $cm^{-1}$ specifically Zn-O and Fe-O bonds, at 609 and 460 $cm^{-1}$, respectively. The peaks at 3782 to 3331 $cm^{-1}$ are attributed to -OH groups from glycine and diethylene glycol, as well as acetate bonds from zinc acetate dihydrate salt [21-23]. Moreover, the O-H stretching vibrations at 1565, 1560 and 1541 $cm^{-1}$, C-H vibration bands at 1392, 1416 and 1320 $cm^{-1}$ and C-O stretching vibration bands at 1031 $cm^{-1}$ and 1045 $cm^{-1}$ were also identified [14,24,25]. The C-O stretching vibration band confirms the binding moieties of diethylene glycol onto $Fe_3O_4$/ZnO nanocomposites. Furthermore, absorption bands at 2073 and 1389 $cm^{-1}$ are due to carbonyl groups. Fig. 3b shows the vibrational and structural properties of the composite nanoparticles. Laser type 532 was used with a low laser power of 5 mW to obtain the spectra of the nanoparticles. Generally, it is known that magnetite is not Raman active, especially at low-power lasers. Therefore, the characteristic peaks of $Fe_3O_4$ corresponded to $E_{2g}$, $A_{1g}$ and $E_{1g}$ which are known to be both Raman and infrared active, the observed results corre-

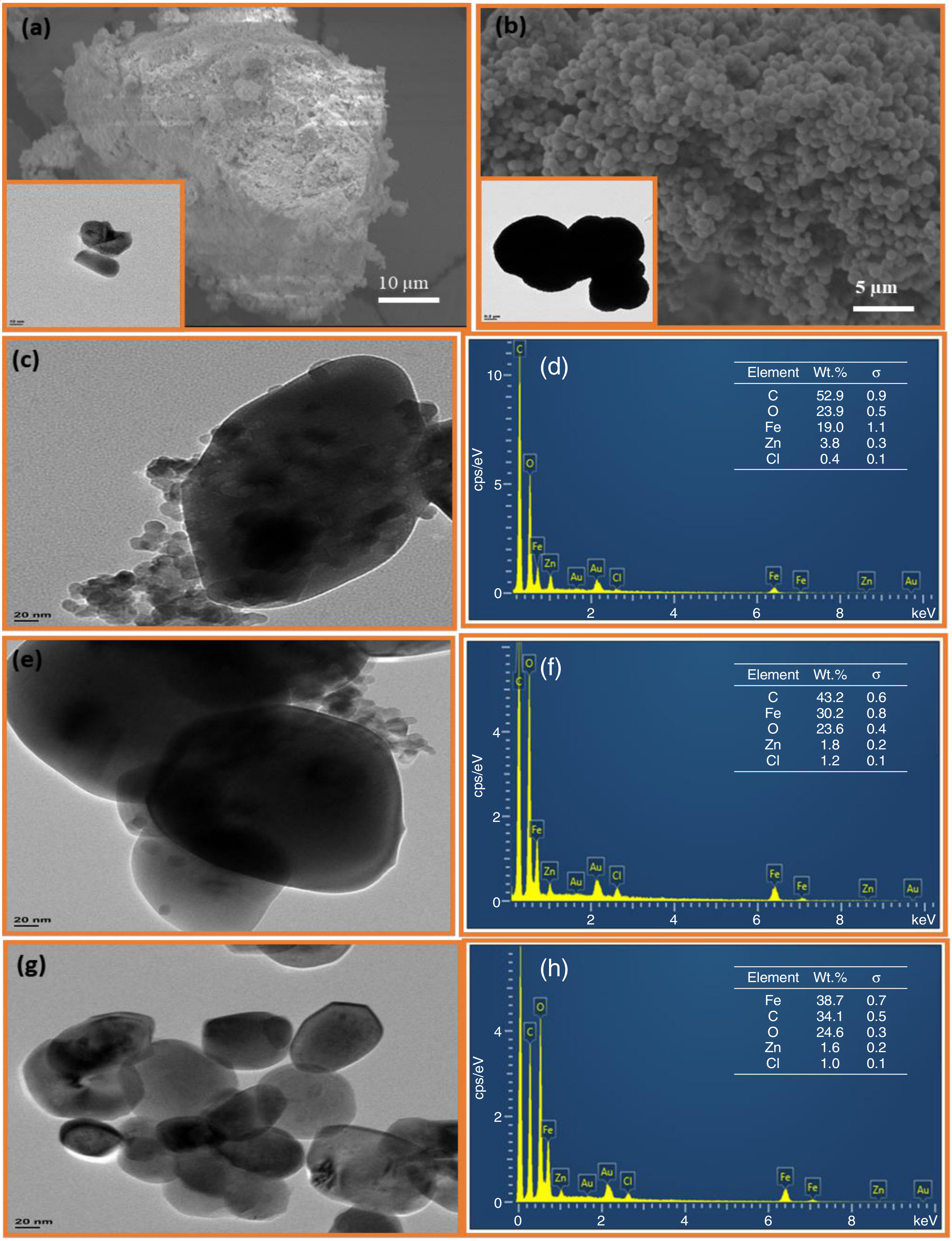

(d)

| Element | Wt.% | σ |
|---|---|---|
| C | 52.9 | 0.9 |
| O | 23.9 | 0.5 |
| Fe | 19.0 | 1.1 |
| Zn | 3.8 | 0.3 |
| Cl | 0.4 | 0.1 |

(f)

| Element | Wt.% | σ |
|---|---|---|
| C | 43.2 | 0.6 |
| Fe | 30.2 | 0.8 |
| O | 23.6 | 0.4 |
| Zn | 1.8 | 0.2 |
| Cl | 1.2 | 0.1 |

(h)

| Element | Wt.% | σ |
|---|---|---|
| Fe | 38.7 | 0.7 |
| C | 34.1 | 0.5 |
| O | 24.6 | 0.3 |
| Zn | 1.6 | 0.2 |
| Cl | 1.0 | 0.1 |

Fig. 1. SEM images and insert HR-TEM images of (a) $Fe_3O_4$, (b) ZnO, HR-TEM and EDX images of (c-d) 1:1, (e-f) 1:2 and (g-h) 2:1 ratio of $Fe_3O_4$/ZnO nanoparticles

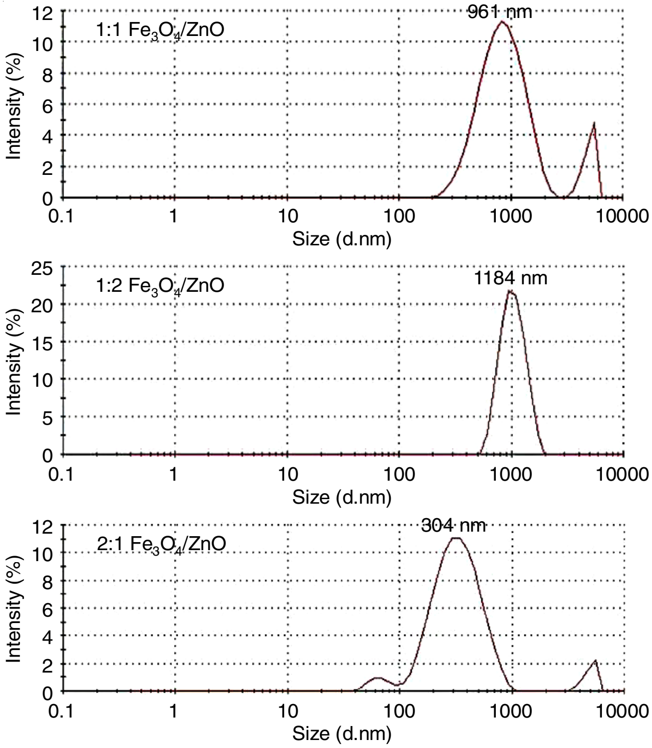

Fig. 2. Zeta sizer analysis of the different mass ratios of $Fe_3O_4$/ZnO nanoparticles

lated with other studies [26]. The peaks observed at 324 and 431 cm$^{-1}$ are attributed to ZnO due to acetate vibrational bonds and oxygen vibration mode [27]. The 1:1 ratio shows a dispersed peak at 94.80 and 608 cm$^{-1}$ while the 1:2 and 2:1 ratio shows a peak at 584 cm$^{-1}$ indicating that the produced nanocomposite is crystal and contained vibrational bonds of both magnetite and hematite. The Fe-doped ZnO appearing at ~ 652 cm$^{-1}$ observed from the 1:1 strongly confirms that the produced $Fe_3O_4$ core is incorporated into the ZnO shell. The results obtained on Raman spectra for $Fe_3O_4$ correlated with the FTIR spectral results and the observed TEM morphologies (Fig. 1).

**XPS and XRD spectral studies:** The X-ray photoelectron spectrometry is a suitable technique to confirm the chemical composition, bonds and surface chemistry of $Fe_3O_4$/ZnO nanoparticles. The survey scan (Fig. 4) confirmed the coexistence of the expected elements in the sample. The peak intensity for the ZnO phase (Zn 2p) is significantly higher compared to that for the $Fe_3O_4$ elements. Generally, the deconvolution of Fe 3p results in the different phases of $Fe^{2+}$ and $Fe^{3+}$ which is commonly observed for the formation of $Fe_3O_4$ [28,29].

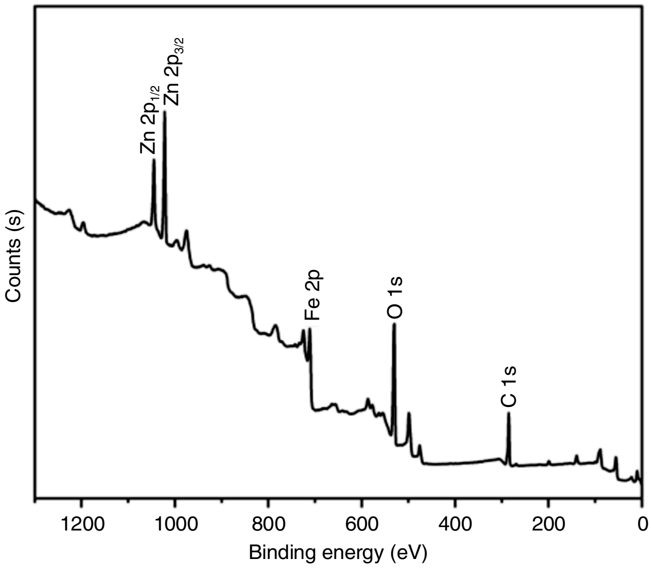

Fig. 4. XPS survey scan of 1:1 $Fe_3O_4$/ZnO nanocomposites

The largest peak in the high-resolution Fe 2p spectra (Fig. 5a) can be attributed to the Fe 2p$^{3/2}$ of $Fe^{2+}$ species, whereas the other two main peaks, at 724.2 and 713.08 eV, are the Fe 2p$^{1/2}$ and Fe 2p$^{3/2}$ of $Fe^{3+}$ species, respectively. The presence of highly crystalline $Fe_3O_4$ in the samples is confirmed by a satellite peak at 717.79 eV. The presence of ZnO (Fig. 5b) was confirmed by the two major peaks with centres at 1021.58 eV and 1044.58

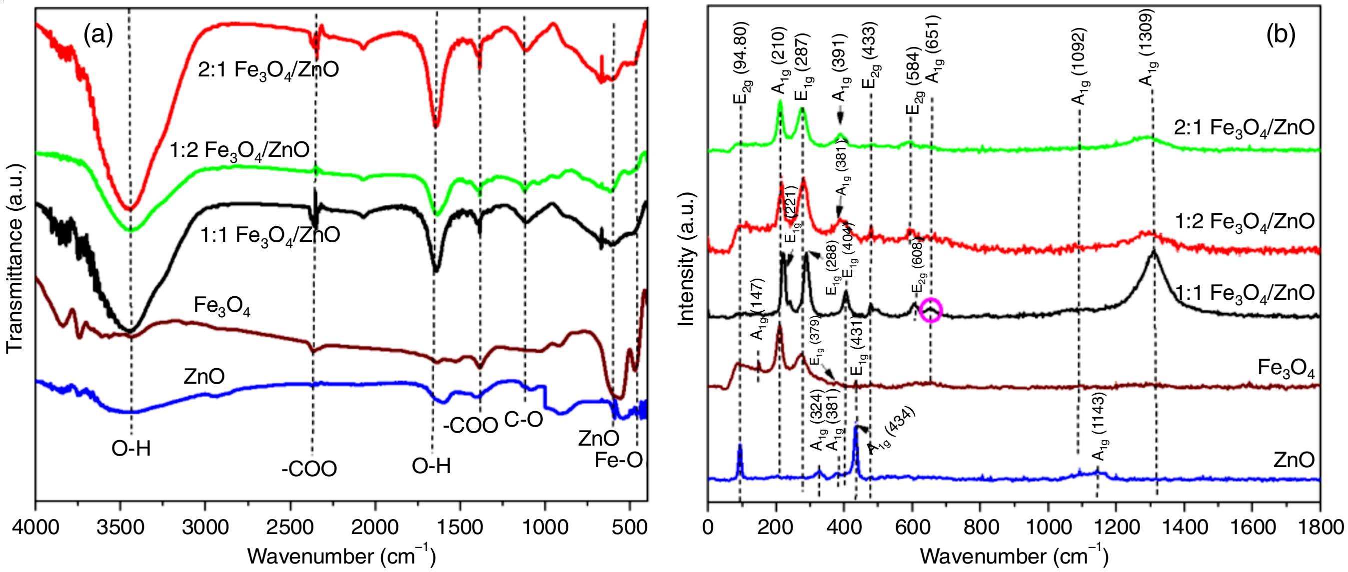

Fig. 3. (a) FTIR and (b) Raman spectra of $Fe_3O_4$/ZnO nanoparticles and nanocomposites in their ratios

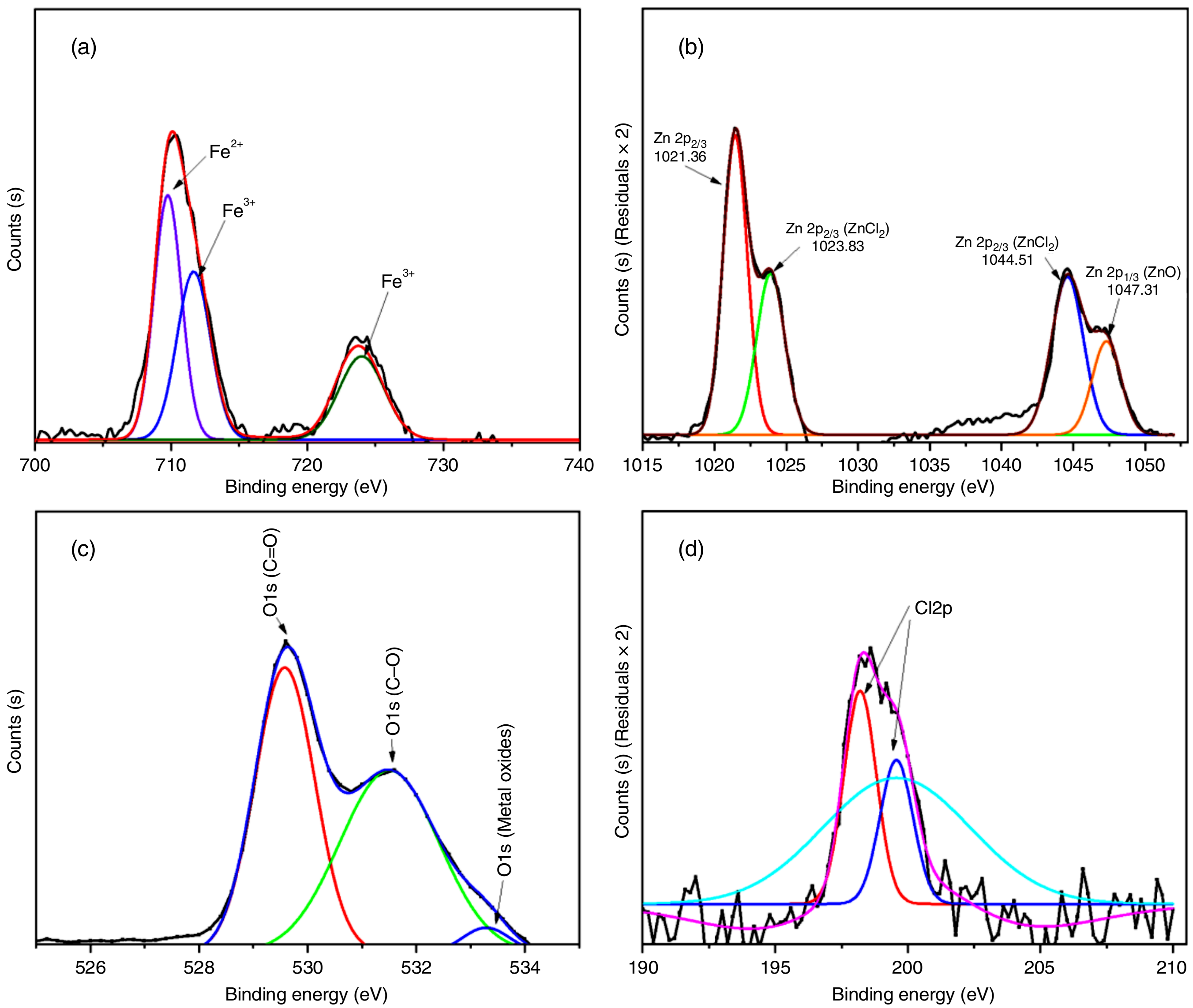

Fig. 5. High-resolution XPS spectra of (a) Fe2p for 1:1 $Fe_3O_4$/ZnO, (b) Zn2p, (c) O1s and (d) Cl2p

eV, respectively, corresponding to Zn $2p^{3/2}$ and Zn $2p^{1/2}$. Interestingly, both Fe 2p and Zn 2p showed a robust satellite structure confirming hybridization between $Fe_3O_4$ and ZnO phases in the heterostructures. The O1s spectrum (Fig. 5c) shows three peaks at 529.68, 531.51 and 533.57 eV, corresponding to carbon monoxide, carboxyl groups and metal oxide bonds (Fe-O and Zn-O), with defects from hydroxyl, carbonate and dioxide groups and the observed findings are similar to other studies [30]. The presence of Zn 2pCl (Fig. 5d) is attributed to the trace of chlorine suggesting that zinc reacts on the surface with chloride from ferric salts and HCl forms species like oxychloride.

The crystallinity of the produced $Fe_3O_4$/ZnO nanocomposites was determined using the X-ray spectroscopy. Fig. 6 showed patterns of functionalized $Fe_3O_4$, ZnO and different ratios of $Fe_3O_4$/ZnO nanoparticles. The diffraction peaks and indexes of $Fe_3O_4$ nanoparticles are confirmed to be planes of a cubic spinel $Fe_3O_4$ crystal similar to JCPDS 96-900-7645 [31]. These indexes correlate well with the XRD findings of Lemes *et al.*

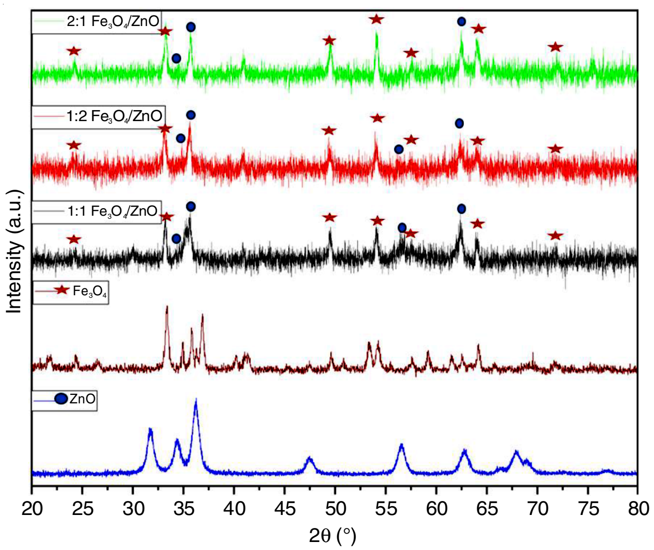

Fig. 6. XRD spectra of the bulk nanoparticles and the different ratios of $Fe_3O_4$/ZnO nanocomposites

[32]. The strong diffraction peaks and indexes for ZnO nanoparticles corresponded to planes of hexagonal wurtzite structure of ZnO with JCPDS 71-6424. The indexes of ZnO nanoparticles obtained correlate to other studies [8,33]. The coexistence of diffraction indexes of both $Fe_3O_4$ and ZnO is observed in the different ratios which indicated the successful incorporation of the nanocomposites confirming the formation of $Fe_3O_4$/ZnO heterostructure. However, the diffraction peak intensity at (002) and (001) attributed by ZnO from the heterostructure decreased with increasing concentration ratio variation suggesting that there are changes in the crystal structures and particle size diameter of the heterostructures. Table-1 showed that an increase in the lattice parameter increased the crystal particle size of the bulk material. The different $Fe_3O_4$/ZnO ratios showed an increase in the $D_{311}$ $Fe_3O_4$ lattice pattern and a decrease in the crystal size of the core nanocomposite while there was no trend observed for the $D_{102}$ ZnO lattice pattern. The shift in lattice d-spacing (311) confirms the existence of the different valence states of Fe ions, this observation confirmed the different phase states of iron oxide from XPS results [34]. The 1:1 nanocomposite ratio suggests that the crystallinity improved compared to the other $Fe_3O_4$/ZnO nanocomposite ratios. Therefore, the effect concentration ratio has an effect on the crystallinity of the $Fe_3O_4$/ZnO nanocomposite heterostructures.

**Optical properties:** Fig. 7 shows the optical properties of the bulk nanoparticles and the different molar ratios of $Fe_3O_4$/ZnO nanocomposite. UV-vis diffuse reflectance spectroscopy was used to determine the shape, size, state of aggregation and concentration of nanoparticles [35]. The bulk $Fe_3O_4$ and ZnO depicted a band edge absorption peak between 547 to 650 nm and 545 to 750 nm [36]. Fig. 7a shows that the 1:1 ratio had a low absorption intensity compared to the 1:2 (2.64 eV) ratio illustrating that it has a higher band gap energy of 2.85 eV as illustrated in Fig. 7b due to the diamagnetic nature of ZnO that tends to reduce the $Fe^{3+}$ cations in the octahedral sites [37]. The 2:1 ratio has the highest absorbance intensity and a low band energy of 2.50 eV compared to the other ratios. This is due to the increment in $Fe_3O_4$ concentration that results in the reduction of defect energy levels of the composite increasing the visible light absorption capability [38].

Generally, the Mie theory predicts an absorption peak of ~377 nm corresponds to the quadrupolar plasmon resonance of spherical nanoshells or spherical nanoparticles [35,38]. According to the results obtained, it is evident that peaks between ~365-369 nm are observed in all different ratios of $Fe_3O_4$/ZnO nanocomposite. The variation of the peak broadness can be due to the quantum size effect. The absorption band edges of all the nanocomposites were blue-shifted. Therefore, nanocomposites can be utilized as a visible light-responsive photocatalyst. These results correspond to other studies [20,37,39]. Overall, Fig. 7b, shows that the bulk nanoparticles had low band gap energies of 2.39 and 2.89 eV. The differentiation in the band gap energies is due to the quantum size effect [40]. The band gap energy is inversely proportional to the size of the nanoparticles

TABLE-1
THE LATTICE SPACING OF (311) OF $Fe_3O_4$ AND (101) OF ZnO WAS USED TO CALCULATE THE CRYSTAL SIZE (nm) OF THE NANOPARTICLES

| Samples | $D_{311}$ $Fe_3O_4$ (Å) | $D_{102}$ ZnO (Å) | $Fe_3O_4$ core (nm) | ZnO shell (nm) | SEM/TEM morphology |
|---|---|---|---|---|---|
| $Fe_3O_4$ | 8.30 | – | 25.38 | – | Cubic |
| ZnO | 3.49 | – | – | 16.00 | Spherical |
| 1:1 $Fe_3O_4$/ZnO | 8.44 | 5.62 | 17.42 | 17.44 | Spherical-cubic |
| 1:2 $Fe_3O_4$/ZnO | 8.98 | 5.63 | 17.32 | 17.44 | Spherical-cubic |
| 2:1 $Fe_3O_4$/ZnO | 8.93 | 5.62 | 17.32 | 17.44 | Spherical-cubic |

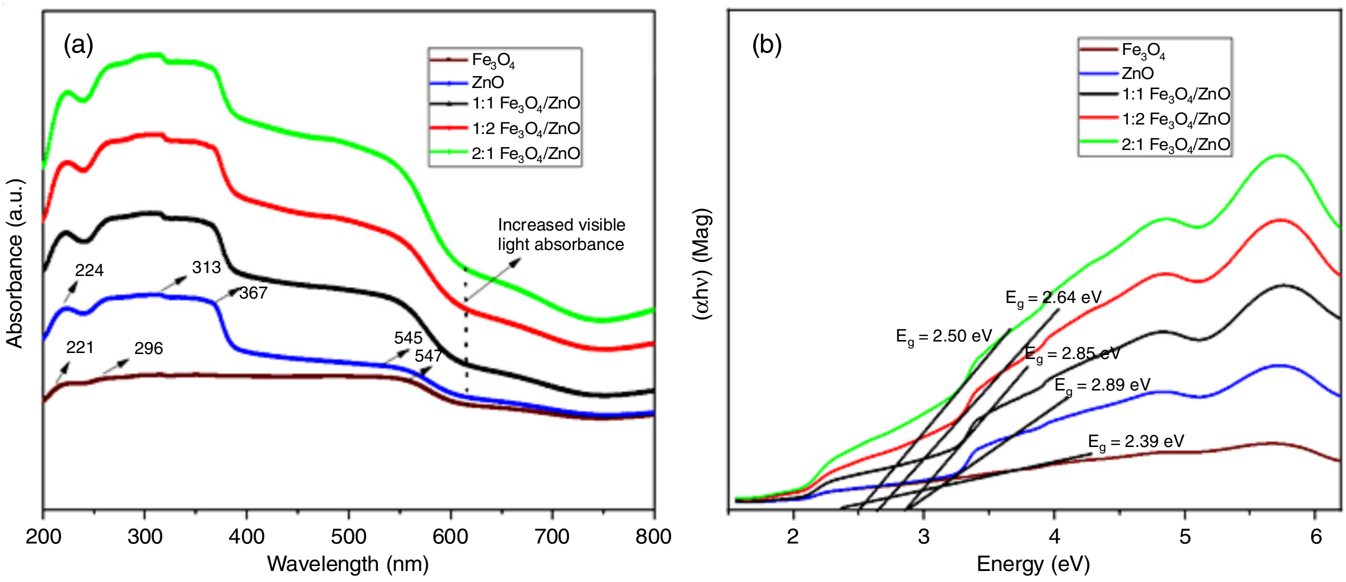

Fig. 7. (a) UV-visible spectra and (b) Tauc plots of $Fe_3O_4$, ZnO and $Fe_3O_4$/ZnO nanocomposites ratios

correlating with the obtained crystal size from XRD (Table-1) and the observed morphology of TEM images (Fig. 1). Therefore, the 1:1 nanocomposite ratio indicates that its visible light absorption is greatly enhanced and can be applied as a photocatalyst [8].

**Photoluminescence (PL) studies:** The PL emission peaks observed at ~350 and 400 nm are associated with the recombination near band edge emission. The PL studies (Fig. 8) were conducted to study the different emission peaks of $Fe_3O_4$/ZnO ratios. It is observed that the bulk $Fe_3O_4$ and ZnO have emission peaks at 364.01 nm and 363.91 nm, the observed intensity increment illustrates that ZnO has a rapid rate of recombination electron-hole pair. The $Fe_3O_4$ and the (1:2 and 2:1ratios) of $Fe_3O_4$/ZnO nanocomposites have lower PL intensity illustrating there is a reduction in the rate of electron-hole pair recombination rate. Fig. 7a illustrates that the rate of recombination electron pair of the nanocomposites increased in the following order: 1:1 (2.85 eV) < 1:2 (2.64 eV) < 2:1 (2.50 eV). The 2:1 nanocomposite had the lowest recombination electron-hole rate. Generally, a lower recombination electron/hole pair rate results in a higher photocatalytic activity, this is due to the attribution of increased concentration of $Fe_3O_4$ preventing the photoinduced electron-hole pair recombination that results in reduced band gap energy. Core-shell $Fe_3O_4$/ZnO nanocomposites ratios of 1:2 and 2:1 had lower emission peaks at 728 nm than the 1:1 $Fe_3O_4$/ZnO nanocomposites ratio and the bulk ZnO nanoparticles. This could be attributed to a decrease in the density of oxygen vacancies near the crystal surface in the ZnO layer that was deposited [41]. The intensity of PL emission varies with the rate of photo-induced electron-hole recombination and the surface oxygen defects can also have an effect on the PL emission. Therefore, from the attained PL results of this study, we observed an increase in PL emission intensity indicating the enhanced photocatalytic activity of the 1:1 nanocomposite ratio, this correlates with other studies [42,43]. Based on the well-defined core-shell structure morphology, Raman spectra and optical properties indicate that the combination of the bulk nanoparticles enhances the photocatalytic activity. Therefore, the 1:1 nanocomposite ratio was further studied for photocatalysis because it displayed a stronger emission peak at 363 nm and 728 nm compared to the other nanocomposites. On the other hand, its band gap energy illustrates that there are ZnO interstitial defects [8,44]. The emission bands of the obtained results are similar to other literature studies [23,44,45].

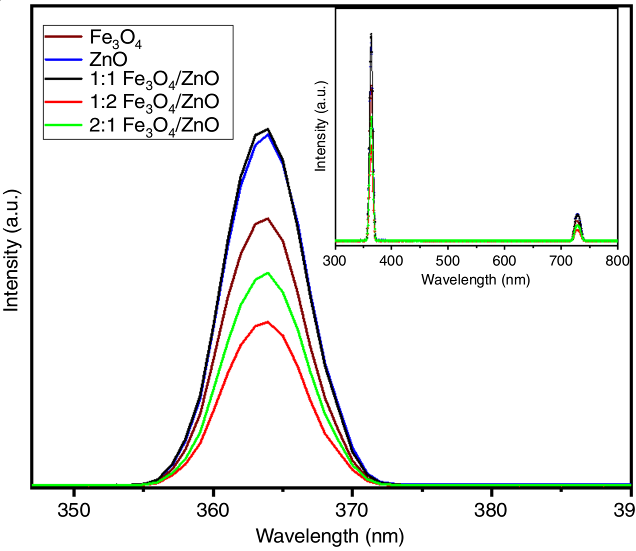

Fig. 8. PL spectral analysis of $Fe_3O_4$/ZnO nanocomposites in their ratios

**BET analysis:** The BET instrument was used to measure the surface area, pore size and pore volume of the nanocomposites . The BHJ method demonstrated that the 1:1 ratio of $Fe_3O_4$/ZnO had a broad pore size distribution compared to the 1:2 and 2:1 ratio (Table-2). Fig. 9a showed an IV-type curve with an H3-type hysteretic loop suggesting that the material is mesoporous and the formed aggregates are of spheres. Fig. 9b-c showed a type III curve suggesting that there are no pores on the surface of the composite nanoparticles. Therefore, the 1:1 ratio can be implemented for both adsorption and photocatalysis studies since it has a higher surface area and mean pore diameter of 94.360 $m^2/g$ and 12.454 nm compared to the other ratios, which could be beneficial for generating catalytic active interactions although the large pore diameter might restrain the electron/hole pairs. Generally, smaller particles result in a high surface area. Therefore, the high surface area of 1:1 ratio correlate well with the particle size diameter obtained from TEM images. These results concurred with Dlugosz *et al.* [46] results.

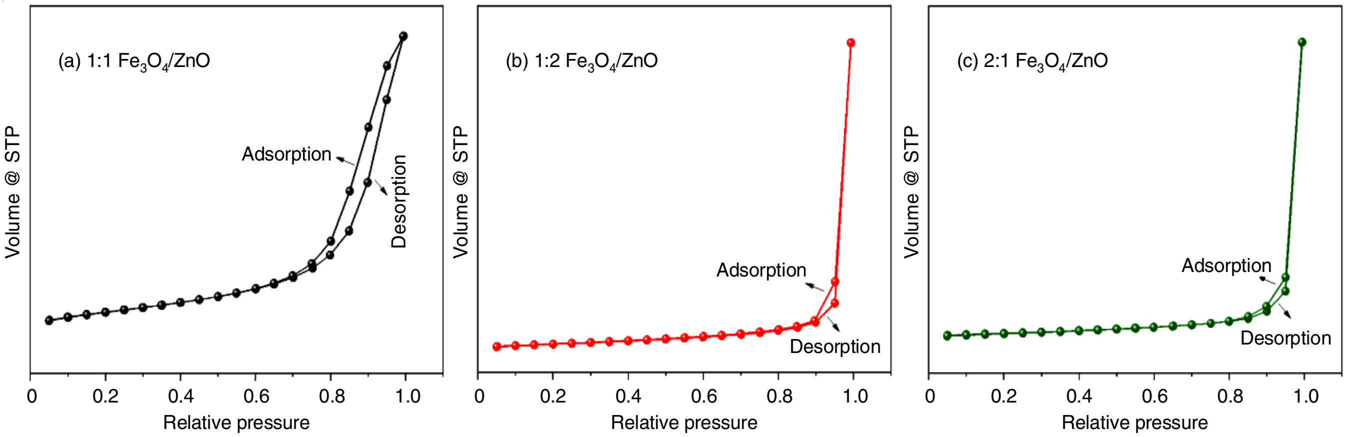

Fig. 9. BET analysis of $Fe_3O_4$/ZnO nanocomposites (1:1, 1:2 and 2:1 ratios) carried under air and nitrogen atmosphere

TABLE-2
SURFACE AREA, PORE VOLUME AND MEAN PORE DIAMETER OF $Fe_3O_4$/ZnO

| Ratio of $Fe_3O_4$/ZnO | BET surface area ($m^2$/g) | Pore volume (cc/g) | Mean pore diameter (nm) |
|---|---|---|---|
| 1:1 | 94.360 | 0.360 | 12.454 |
| 1:2 | 12.595 | 0.221 | 1.7047 |
| 2:1 | 14.537 | 0.276 | 1.7067 |

**EIS studies:** The EIS Nyquist plots (Fig. 10) of $Fe_3O_4$/ZnO nanocomposites show that the ratio 1:1 had a smaller charge carrier transfer resistance compared to the other ratios suggesting that it possessed superior electrochemical conductivity. This further illustrates that the 1:1 ratio can induce efficient separation and help the photogenerated electron-hole pairs that could enhance the photocatalytic activity for the degradation of RhB dye. These observations are similar to Varadi *et al.* [47]. The observed findings correlate with the BET results showing that the 1:1 ratio of $Fe_3O_4$/ZnO nanocomposites possessed more anchored sites for mass transfer and light absorption. It also correlated to the XPS analysis (Fig. 5a) showing the redox species of $Fe^{2+}/Fe^{3+}$, the redox reactions are known to promote the migration of electrons which are favourable for photocatalytic process.

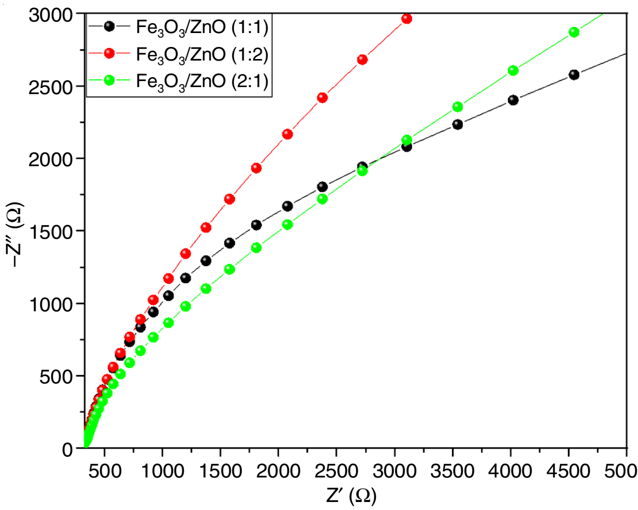

Fig. 10. EIS Nyquist plots of $Fe_3O_4$/ZnO nanocomposites (1:1, 1:2 and 2:1 ratio)

**Photocatalytic performance of modified $Fe_3O_4$/ZnO nanoparticles:** In general, photocatalytic activity reactions occur between the surfaces of the catalyst and the contaminant, therefore, are dependent on the morphological structure and optical properties of catalyst [48]. The photocatalytic activity of RhB dye was monitored under both solar light and visible light irradiation using a modified $Fe_3O_4$/ZnO photocatalyst. Generally, experiments are conducted in dark for 1 h to attain adsorption equilibrium. Fig. 11a-b show the absorption spectra of RhB dye under the presence of the photocatalyst after photodegradation with different time intervals. Fig. 11a shows that the composite ratio exhibited the highest removal efficiency for RhB under visible light at 180 min compared to RhB under solar light (Fig. 11b). The maximum removal efficiency of RhB at 180 min under visible and solar is observed to be 83.81% and 29.87%. This high degradation efficiency indicates that the 1:1 ratio contained a high surface area (94.360 $m^2$/g) with the effective charge separation efficiency of charge carriers. This confirms that the modified catalyst played an important role in supplying photogenerated carriers trapping sites that captured RhB under visible light.

Table-3 shows that there are limited research studies that focus on the co-precipitation approach for producing core-shell structures of $Fe_3O_4$/ZnO nanocomposites for the degradation of RhB dyes under visible light. It also indicates that synthesized 1:1 $Fe_3O_4$/ZnO nanocomposites can effectively degrade 83.81% RhB dye at 180 min. Therefore, this performance is higher compared to similar catalyst prepared previously by other researchers [12,13]. Although $Fe_3O_4$/ZnO nanocomposites prepared in this study used fewer resources, its performance is comparable to catalysts that have been enhanced using additional nanoparticles to enhance their photodegradation performance [9,49]. Therefore, this indicates that it is a cost efficient photocatalyst.

**FTIR studies before and after degradation:** FTIR analysis was conducted to determine the structural changes of $Fe_3O_4$/ZnO nanocomposite catalyst before and after sorption studies. The RhB dye Fig. 12a shows C-O stretching (1112.02 $cm^{-1}$), C-C stretching (1327.59 and 1383.922 $cm^{-1}$), C-N stretching (3472.19 $cm^{-1}$), C=C stretching (3248.27 $cm^{-1}$), C-H stretching (2127.99 $cm^{-1}$), C=O from amide stretching (1616.65 $cm^{-1}$) aromatic groups (1383.92 $cm^{-1}$), confirming the structure of

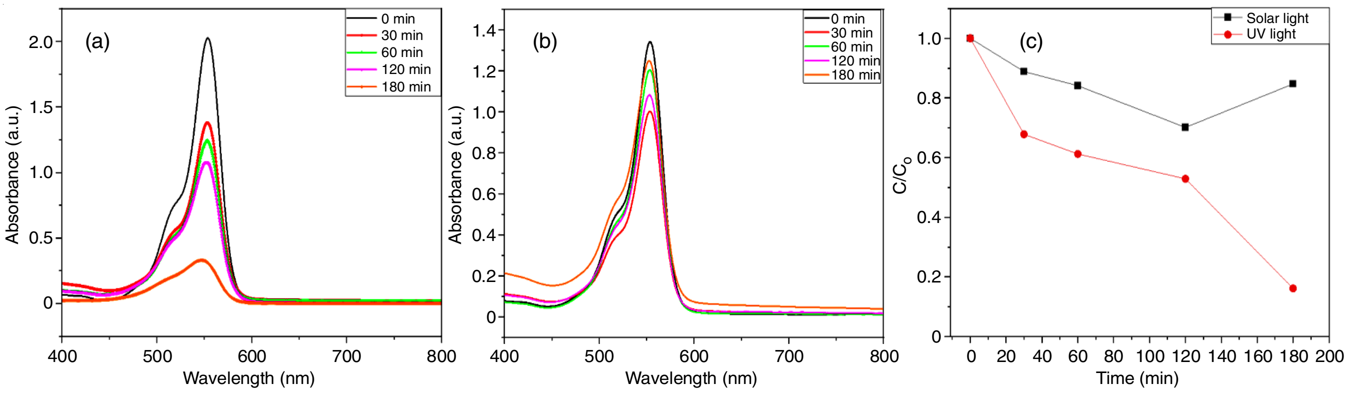

Fig. 11. Absorbance of 1:1 $Fe_3O_4$/ZnO nanoparticles under (a) visible light, (b) solar light for the desorption of RhB dye and (c) degradation rate of the photocatalytic activity

TABLE-3
COMPARISON STUDIES FOR THE DEGRADATION OF RHODAMINE B DYE

| Catalyst | Synthesis method | Dye | Irradiation | Degradation time (min) | Degradation efficiency (%) | Ref. |
|---|---|---|---|---|---|---|
| $Fe_3O_4$/ZnO@ZIF-8 | Hydrothermal | Rhodamine B | Visible | 100 | 98.00 | [9] |
| $Fe_3O_4$/ZnO nanoparticles | Co-precipitation | Methyl orange | Visible | 240 | 22.00 | [12] |
| $Fe_3O_4$/ZnO | Co-precipitation | Methylene blue | Visible | 360 | 20.00 | [13] |
| $Fe_3O_4$/ZnO-Cu nanocomposite | Co-precipitation | Rhodamine B | Visible | 120 | 89.41 | [49] |
| $Fe_3O_4$/ZnO nanocomposite | Coprecipitation | Rhodamine B | Visible | 180 | 83.81 | Present study |

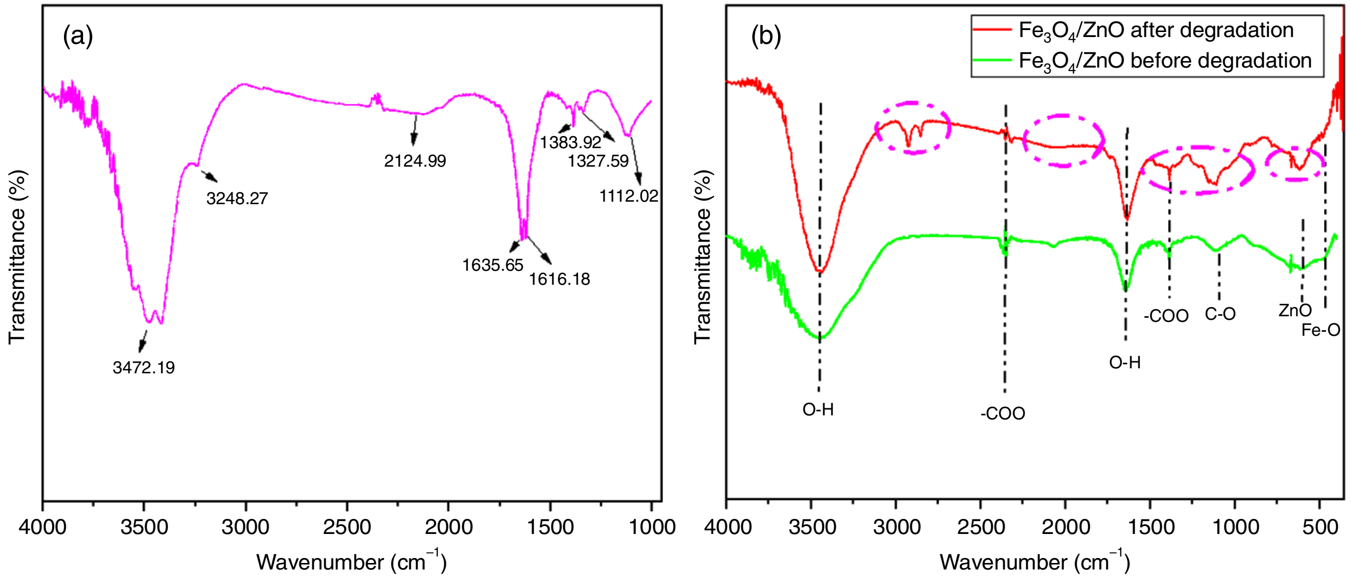

Fig. 12. FTIR spectra of (a) rhodamine B dye and 1:1 $Fe_3O_4$/ZnO nanocomposite before and after degradation of RhB under visible light

RhB dye. After degradation, the FTIR spectrum (Fig. 12b) shows an increase in the bands at 3782, 1635.65, 1383.92 and 609 cm$^{-1}$, which indicates that there was sorption of RhB dye and subsequently the appearance of bands at 2919.63, 2848.63, 2068.63, 1456.97, 947.13 cm$^{-1}$ confirms the functional groups of RhB dye [50,51].

**Mechanism of RhB dye photodegradation:** Based from the obtained results, the proposed mechanism for the photodegradation of RhB utilizing $Fe_3O_4$/ZnO nanocomposite is shown in Fig. 13. Magnetite plays a critical role as an electron transfer and acceptor channel due to its good conductivity and the presence of $Fe^{2+}$/ $Fe^{3+}$. When visible light is irradiated on both ZnO and $Fe_3O_4$ absorbs photon energy and electrons are transferred from the valence band to the conduction band. The Mulliken electronegativity theory was used to calculate the valence band (VB, $E_{VB}$) and conduction band (CB, $E_{CB}$) potentials using eqns. 1 and 2 [10]. To understand photocatalysis, the band gap energies of ZnO and $Fe_3O_4$ were 2.39 eV and 2.89 eV.

$$E_{CB} = X - E^e - \frac{1}{2}E_g \tag{1}$$

$$E_{VB} = E_g + E_{CB} \tag{2}$$

In this equation, X represents the absolute electronegativity of semiconductors (X for ZnO = 5.78 eV and $Fe_3O_4$ = 5.73 eV), $E^e$ and $E_g$ is the energies of the free electrons on the hydrogen scale (4.50 eV) and band gap energies of the bulk nanomaterials. The calculated $E_{CB}$ and $E_{VB}$ for ZnO are -0.19 and 3.08 eV, respectively, whereas $Fe_3O_4$ are 0.085 and 1.54 eV, respectively. The standard potential of standard redox potential of $HO^{\bullet}/H_2O$ (2.73 eV *vs.* NHE), $O_2/^{\bullet}O_2$ (-0.33 eV *vs.* NHE) and $O_2/H_2O_2$ (0.80 eV *vs.* NHE). Photogenerated electrons from the conduction band of ZnO are transferred to the conduction band of $Fe_3O_4$ nanoparticles at the composite surface and then react with the surface peroxide to generate hydroxyl radicals. The holes retained in the valence band of ZnO NPs react directly with RhB dye and are also transferred into the valence band of $Fe_3O_4$. The VB position of ZnO is larger than the standard redox potential of $HO^{\bullet}/H_2O$ and conduction band of $O_2/H_2O_2$ radicals is more positive than the standard redox. Hence, the formation of OH radicals occurs at the valance band of ZnO when holes in the valance band combine with $H_2O$ molecules. The photo-induced conduction band electrons of ZnO and $Fe_3O_4$ cannot reduce $O_2/^{\bullet}O_2$ radicals therefore, dissociate into reactive OH radicals. Thereafter, the RhB dye is degraded by the holes and hydroxyl radicals to form eco-friendly inorganic byproducts of $H_2O$ and $CO_2$ molecules. The predicted mechanism is as follows:

$$h\nu + \text{Photocatalyst surface} \rightarrow e^-_{CB} + h^+_{VB} \tag{3}$$

$$^{\bullet}O_2 + 2H^+ \rightarrow 2HOO^{\bullet} \rightarrow H_2O_2 \tag{4}$$

$$H_2O_2 + e^- + H^+ \rightleftharpoons HO + H_2O \tag{5}$$

$$h^+_{VB} + H_2O \rightarrow H^+ + {}^{\bullet}OH \tag{6}$$

$$^{\bullet}OH + RhB \rightarrow CO_2 + H_2O \text{ (Degradation products)} \tag{7}$$

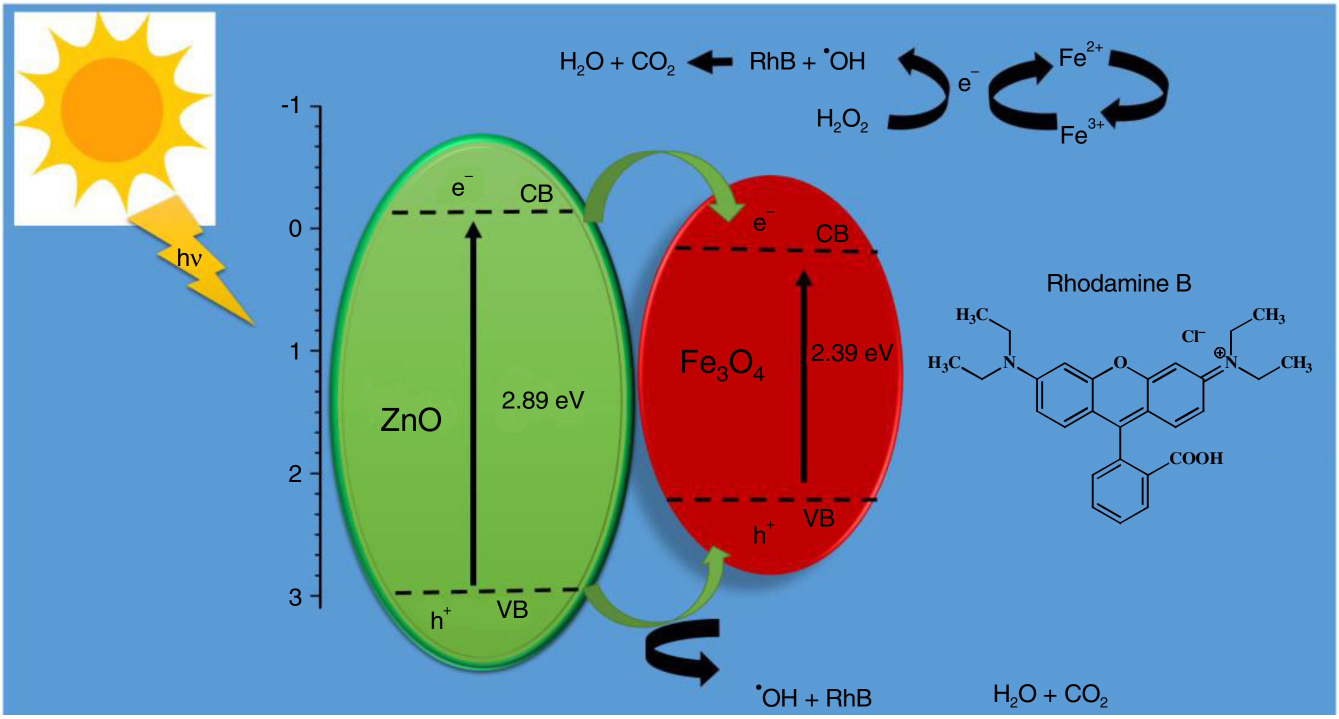

Fig. 13. Possible schematic diagram of RhB degradation using $Fe_3O_4$/ZnO nanocomposite as a photocatalyst

## Conclusion

Core-shell $Fe_3O_4$/ZnO nanocomposites ratios (1;1, 1:2 and 2:1) were successfully synthesized using the co-precipitation method. The pH, particle size and morphology of the ratios contribute to the formation of the core-shell nanocomposites for the efficient degradation of RhB dye molecules. TEM images confirmed that the synthesized nanocomposites consist of core-shell structures. The elemental components, functional groups and vibrational modes showed distinct features of all the expected functional groups. The optical properties revealed that the 1:1 molar ratio had a large band gap of 2.85 eV. Therefore, the prepared modified nanoparticles can be used as a responsive photocatalyst for the removal of organic matter and heavy metals present in wastewater. The BET results showed that the characteristic hysteresis loop of the 1:1 ratio was a composition of spheres. A comparative degradation of RhB dye using UV-visible light and solar irradiation for the 1:1 $Fe_3O_4$/ZnO nanocomposite revealed that degradation of RhB dye under visible light exhibited the highest degradation efficiency. Therefore, further studies can be conducted to understand the interaction of the active sites responsible for the degradation of RhB dye, the photoelectrochemical properties and explore the efficiency of the 1:1 ratio on other dyes, pharmaceuticals and environmental water samples.

## ACKNOWLEDGEMENTS

The authors would like to extend their acknowledgments to the Institute for Nanotechnology and Water Sustainability (iNanoWS) of the University of South Africa for funding this work. The National Research Foundation (South Africa) is also gratefully thanked for funding.

## CONFLICT OF INTEREST

The authors declare that there is no conflict of interests regarding the publication of this article.

## REFERENCES

1. H. Shayesteh, A. Rahbar-Kelishami and R. Norouzbeigi, *J. Mol. Liq.*, **221**, 1 (2016); https://doi.org/10.1016/j.molliq.2016.05.053
2. M.A. Albo Hay Allah, H.K. Ibrahim, H.A. Alshamsi and H. Radhi Saud, *J. Photochem. Photobiol. Chem.*, **449**, 115413 (2024); https://doi.org/10.1016/j.jphotochem.2023.115413
3. A. Lesniewicz and A. Lewandowska-Andralojc, *Sci. Rep.*, **14**, 22600 (2024); https://doi.org/10.1038/s41598-024-73586-3
4. A. Anjali, Gupta, B. Tripathi, M. Sahni, K. Sharma, N. Ranjan, M.Z.A. Yahya, I.M. Noor and S. Pandit, *Ionics*, **30**, 8267 (2024); https://doi.org/10.1007/s11581-024-05843-4
5. Parul, K. Kaur, R. Badru, P.P. Singh and S. Kaushal, *J. Environ. Chem. Eng.*, **8**, 103666 (2020); https://doi.org/10.1016/j.jece.2020.103666
6. A. Balapure, J.R. Dutta and R. Ganesan, *RSC Appl. Interf.*, **1**, 43 (2024); https://doi.org/10.1039/D3LF00126A
7. M. Xu, Q. Li and H. Fan, *Adv. Powder Technol.*, **25**, 1715 (2014); https://doi.org/10.1016/j.apt.2014.06.019
8. H.L. Pham, V.D. Nguyen, V.K. Nguyen, T.H.P. Le, N.B. Ta, D.C. Pham, Q.T. Tran and V.T. Dang, *RSC Adv.*, **11**, 22317 (2021); https://doi.org/10.1039/D1RA03468E
9. R. Yu, Y. Shang, X. Zhang, J. Liu, F. Zhang, X. Du, H. Sun and J. Zeng, *Catal. Commun.*, **174**, 106583 (2023); https://doi.org/10.1016/j.catcom.2022.106583
10. N. Madima, K.K. Kefeni, S.B. Mishra, A.K. Mishra and A.T. Kuvarega, *Inorg. Chem. Commun.*, **145**, 109966 (2022); https://doi.org/10.1016/j.inoche.2022.109966
11. Y. Wang, X. Li, Y. Yang, J. Yang, N. Zhang, X. Wu and X. Li, *J. Mater. Sci. Mater. Electron.*, **31**, 5187 (2020); https://doi.org/10.1007/s10854-020-03078-3

12. S.D. Kulkarni, S.M. Kumbar, S.G. Menon, K.S. Choudhari and C. Santhosh, *Adv. Sci. Lett.*, **23**, 1724 (2017); https://doi.org/10.1166/asl.2017.8484
13. S. Chidambaram, B. Pari, N. Kasi and S. Muthusamy, *J. Alloys Compd.*, **665**, 404 (2016); https://doi.org/10.1016/j.jallcom.2015.11.011
14. R. Elshypany, H. Selim, K. Zakaria, A.H. Moustafa, S.A. Sadeek, S.I. Sharaa, P. Raynaud and A.A. Nada, *Molecules*, **26**, 2269 (2021); https://doi.org/10.3390/molecules26082269
15. P. Goyal, S. Chakraborty and S.K. Misra, *Environ. Nanotechnol. Monit. Manag.*, **10**, 28 (2018); https://doi.org/10.1016/j.enmm.2018.03.003
16. K.K. Nishad, N. Tiwari and R.K. Pandey, *J. Electron. Mater.*, **47**, 3440 (2018); https://doi.org/10.1007/s11664-018-6171-3
17. J.C. Sin, S.Q. Tan, J.A. Quek, S.M. Lam and A.R. Mohamed, *Mater. Lett.*, **228**, 207 (2018); https://doi.org/10.1016/j.matlet.2018.06.027
18. D.N. Tukan, L. Rosmainar, K. Kustomo and R. Rasidah, *J. Berkala Ilmiah Sains Terapan Kimia*, **17**, 15 (2023); https://doi.org/10.20527/jstk.v17i2.15134
19. X. Guo and G. He, *J. Mater. Chem. A Mater. Energy Sustain.*, **11**, 11987 (2023); https://doi.org/10.1039/D3TA01904G
20. S.M. Devi, A. Nivetha and I. Prabha, *J. Supercond. Nov. Magn.*, **33**, 3893 (2020); https://doi.org/10.1007/s10948-020-05607-x
21. H. Peng, C. Hu, J. Hu, T. Wu and X. Tian, *J. Sol-Gel Sci. Technol.*, **80**, 133 (2016); https://doi.org/10.1007/s10971-016-4060-x
22. M. Roeinfard and A. Bahari, *J. Supercond. Novel Magn.*, **30**, 3541 (2017); https://doi.org/10.1007/s10948-017-4154-x
23. Shashank, H.S.B. Naik, G. Nagaraju, R.S. Keri, M.M. Naik and K. Lingaraju, *J. Electron. Mater.*, **50**, 3557 (2021); https://doi.org/10.1007/s11664-021-08816-9
24. H.N. Ulya, A. Taufiq and Sunaryono, *IOP Conf. Ser. Earth Environ. Sci.*, **276**, 2 (2019); https://doi.org/10.1088/1755-1315/276/1/012059
25. A. Kolodziejczak-radzimska, E. Markiewicz and T. Jesionowski, *J. Nanomater.*, **2012**, 656353 (2012); https://doi.org/10.1155/2012/656353
26. P.P.C. Bergmann, *J. Mar. Sci. Eng.*, **5**, 4 (2015); https://doi.org/10.4172/2169-0022.1000217
27. M. Šæepanovic, M. Grujic-Brojèin, K. Vojisavljevic, S. Bernik and T. Sreækovic, *J. Raman Spectrosc.*, **41**, 914 (2010); https://doi.org/10.1002/jrs.2546
28. A.P. Grosvenor, B.A. Kobe, M.C. Biesinger and N.S. McIntyre, *Surf. Interface Anal.*, **36**, 1564 (2004); https://doi.org/10.1002/sia.1984
29. V. Mihalache, C. Negrila, M. Secu, I. Mercioniu, N. Iacob and V. Kuncser, *Results Phys.*, **51**, 106644 (2023); https://doi.org/10.1016/j.rinp.2023.106644
30. B.S. Mun, Z. Liu, M.A. Motin, P.C. Roy and C.M. Kim, *Int. J. Hydrogen Energy*, **43**, 8655 (2018); https://doi.org/10.1016/j.ijhydene.2018.03.155
31. M. Dawn, M. Zzaman, F. Faizal, C. Kiran, A. Kumari, R. Shahid, C. Panatarani, I.M. Joni, V.K. Verma, S.K. Sahoo, K. Amemiya and V.R. Singh, *Braz. J. Phys.*, **52**, 99 (2022); https://doi.org/10.1007/s13538-022-01102-x
32. M.A. Lemes, M.S. Godinho, D. Rabelo, F.T. Martins, A. Mesquita, F.N. De Souza Neto, O.A. Araujo and A.E. De Oliveira, *Acta Chim. Slov.*, **61**, 778 (2014).
33. J. Siregar, K. Sebayang, B. Yuliarto and S. Humaidi, *AIP Conf. Proc.*, **2221**, 110008 (2020); https://doi.org/10.1063/5.0003210
34. S. Karamat, R.S. Rawat, P. Lee, T.L. Tan and R.V. Ramanujan, *Prog. Nat. Sci.*, **24**, 142 (2014); https://doi.org/10.1016/j.pnsc.2014.03.009
35. J. Grand, B. Auguié and E.C. Le Ru, *Anal. Chem.*, **91**, 14639 (2019); https://doi.org/10.1021/acs.analchem.9b03798
36. S.H. Chaki, T.J. Malek, M.D. Chaudhary, J.P. Tailor and M.P. Deshpande, *Adv. Nat. Sci: Nanosci. Nanotechnol.*, **6**, 035009 (2015); https://doi.org/10.1088/2043-6262/6/3/035009
37. A. Taufik, I.K. Susanto and R. Saleh, *J. Phys. Conf. Ser.*, **1091**, 012010 (2018); https://doi.org/10.1088/1742-6596/1091/1/012010
38. A. Roychowdhury, S.P. Pati, A.K. Mishra, S. Kumar and D. Das, *J. Phys. Chem. Solids*, **74**, 811 (2013); https://doi.org/10.1016/j.jpcs.2013.01.012
39. P. Basnet, D. Samanta, T.I. Chanu, S. Jha and S. Chatterjee, *J. Mater. Sci. Mater. Electron.*, **31**, 2949 (2020); https://doi.org/10.1007/s10854-019-02839-z
40. V.A.R. Villegas, J.I. De León Ramírez, E. Hernandez-Guevara, S. Perez Sicairos, L.A. Hurtado-Ayala and B. Landeros-Sanchez, *J. Saudi Chem. Soc.*, **24**, 223 (2020); https://doi.org/10.1016/j.jscs.2019.12.004
41. J.C. Beltran-Huarac, S.P. Singh, M.S. Tomar, S. Peña, L. Rivera and O.J. Perales-Perez, *MRS Online Proc. Lib.*, **1257**, 67 (2010); https://doi.org/10.1557/PROC-1257-O06-04
42. J. Liqiang, Q. Yichun, W. Baiqi, L. Shudan, J. Baojiang, Y. Libin, F. Wei, F. Honggang and S. Jiazhong, *Sol. Energy Mater. Sol. Cells*, **90**, 1773 (2006); https://doi.org/10.1016/j.solmat.2005.11.007
43. L. Jing, *Sci. China B Chem.*, **48**, 25 (2005); https://doi.org/10.1360/03yb0191
44. D. Liu, L. Tong, J. Shi, X. Yang and H. Yang, *J. Mater. Sci. Mater. Electron.*, **23**, 464 (2012); https://doi.org/10.1007/s10854-011-0417-7
45. S. Wang, J. Yang, J. Li, X. Wang, D. Wei, B. Song, H. Li and X. Fu, *Physica E*, **75**, 66 (2016); https://doi.org/10.1016/j.physe.2015.08.040
46. O. Dlugosz, K. Szostak, M. Krupiñski and M. Banach, *Int. J. Environ. Sci. Technol.*, **18**, 561 (2021); https://doi.org/10.1007/s13762-020-02852-4
47. S. Varadi, C. Leostean, M. Stefan, A. Popa, D. Toloman, S. Pruneanu, S. Tripon and S. Macavei, *Inorganics*, **12**, 119 (2024); https://doi.org/10.3390/inorganics12040119
48. J. Ai, C. Lin, W. Liao, C. Hu, T. Zhou, S. Luo, L. Cheng, Z. Chen, Y. Yang, Y. Zhang and W. Li, *Mater. Sci. Technol.*, **35**, 336 (2019); https://doi.org/10.1080/02670836.2018.1558578
49. Y. Pujiarti, E. Suyanta and E.S. Kunarti, *Key Eng. Mater.*, **884**, 60 (2021); https://doi.org/10.4028/www.scientific.net/KEM.884.60
50. P.C. Vithalani and N.S. Bhatt, *Environ. Ecol.*, **40**, 2258 (2022).
51. A. Gulpiya, Z. Su and H. Pan, *J. Austr. Ceram. Soc.*, **57**, 91 (2021); https://doi.org/10.1007/s41779-020-00508-7